Controlling the reactivity of $[Pd^{(II)}(N^\wedge N^\wedge N)Cl]^+$ complexes using 2,6-bis(pyrazol-2-yl)pyridine ligands for biological application: Substitution reactivity, CT-DNA interactions and *in vitro* cytotoxicity study

Daniel O. Onunga [a,f,*], Rajesh Bellam [a], Gershom K. Mutua [a,b], Meshack Sitati [a,g], Manickam D. BalaKumaran [c], Deogratius Jaganyi [d,e,**], Allen Mambanda [a]

[a] *School of Chemistry and Physics, University of KwaZulu-Natal, Private Bag X01, Scottsville, Pietermaritzburg 3209, South Africa*
[b] *Department of Pure and Applied Chemistry, Masinde Muliro University of Science and Technology, P.O. Box 190, Kakamega 50100, Kenya*
[c] *Department of Biotechnology, Dwaraka Doss Goverdhan Doss Vaishnav College, Arumbakkam, Chennai 600106, Tamil Nadu, India*
[d] *School of Pure and Applied Sciences, Mount Kenya University, P.O. Box 342-01000, Thika, Kenya*
[e] *Department of Chemistry, Durban University of Technology, P.O. Box 1334, Durban 4000, South Africa*
[f] *Department of Chemistry, Maseno University, P.O. Box 333-40105, Maseno, Kenya*
[g] *Department of Mathematics and Physical Sciences, Maasai Mara University, P.O. Box 861 Narok 20500, Kenya*

ARTICLE INFO

ABSTRACT

Four $[(N^\wedge N^\wedge N)Pd^{(II)}Cl]^+$ complexes [chloride-(2,2′:6′,2′′-terpyridine)Pd(II)]Cl (**PdL1**), [chlorido(2,6-bis(*N*-pyr-azol-2-yl)pyridine)Pd(II)]Cl (**PdL2**), [chlorido(2,6-bis(3,5-dimethyl-*N*-pyrazol-2-yl)pyridine)Pd(II)]Cl (**PdL3**) and [chlorido(2,6-bis(3,5-dimethyl-*N*-pyrazol-2-ylmethyl)pyridine)Pd(II)]BF$_4$ (**PdL4**) were synthesized and characterized. The rates of substitution of these Pd(II) complexes with thiourea nucleophiles *viz*; thiourea (Tu), *N,N′*-dimethylthiourea (Dmtu) and *N,N,N′,N′*-tetramethylthiourea (Tmtu) was investigated under *pseudo* first-order conditions as a function of nucleophile concentration [Nu] and temperature using the stopped-flow technique. The observed rate constants vary linearly with [Nu]; $k_{obs} = k_2[Nu]$ and decreased in the order: **PdL1** > **PdL2** > **PdL3** ≫ **PdL4**. The lower π-acceptability of the *cis*-coordinated *N*-pyrazol-2-yl groups (which coordinates *via* pyrazollic-N π-donor atoms) of the **PdL2–4** significantly decelerates the reactivity relative to **PdL1**. Furthermore, the six-membered chelates having methylene bridge in **PdL4** do not allow π-extension in the ligand and introduces steric hindrance further lowering the reactivity. Trends in DFT calculated data supported the observed reactivity trend. Spectrophotometric titration data of complexes with calf thymus DNA (CT-DNA) and viscosity measurements of the resultant mixtures suggested that associative interactions occur between the complexes and CT-DNA, likely through groove binding with high binding constants ($K_b = 10^4$ M^{-1}). *In vitro* MTT [3-(4,5-dimethylthiazol-2-yl)-2,5-diphenyltetrazolium bromide] cytotoxic activity data showed that **PdL1** was the most potent complex against MCF7 breast cancer cells; its IC$_{50}$ value is lower than that of cisplatin. The results demonstrate how modification of a spectator ligand can be used to slow down the reactivity of Pd(II) complexes. This is of special importance in controlling drug toxicity in both pharmaceutical and biomedical applications.

1. Introduction

Pd(II) and Pt(II) ions form predominantly square-planar complexes [1]. These complexes and those of other platinum group metal ions have shown great potential for anti-tumour activity, making them useful in chemotherapy [2–6]. For example, Pt(II) complexes such as carboplatin, oxaliplatin and cisplatin have been used for the treatment of ovarian and testicular cancer [7–10]. Some of these drugs have shown serious side effects such as nausea, vomiting, nephrotoxicity, neurotoxicity and ototoxicity [8,11]. The research into alternative non-platinum drugs with high efficacy, less side effects and that can be administered orally is ongoing.

---

* Corresponding author.
** Correspondence to: School of Pure and Applied Sciences, Mount Kenya University, P.O. Box 342-01000, Thika, Kenya.
E-mail addresses: donugake@yahoo.com (D.O. Onunga), deojaganyi@gmail.com (D. Jaganyi).
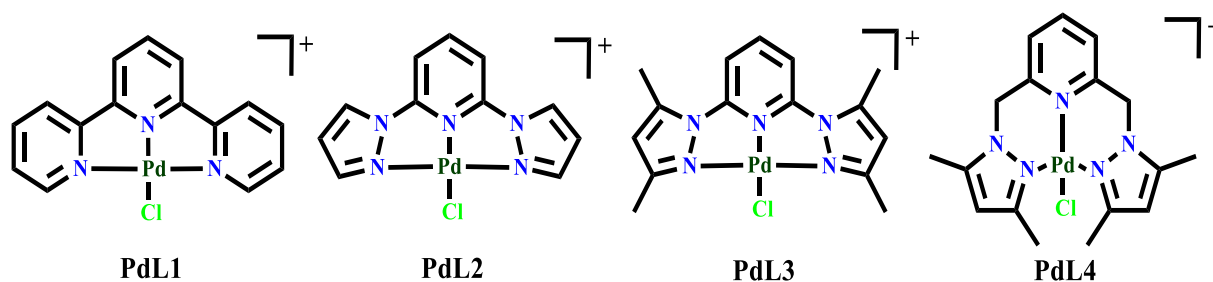
Fig. 1. Structures of complexes, **PdL1**–**4** (counter ions omitted).

Carefully designed Pd(II) complexes can be promising alternatives for chemotherapy; some of them have been reported to be antitumor active [12–20]. Others [21] have shown activity on some cisplatin-resistance tumours. In general, the synthetic design of these Pd(II) antitumor agents follows the same strategies that have been used to design Pt(II) antitumor drugs [22]. Pt(II) and Pd(II) complexes are very similar in their structures and reaction mechanisms. However, their rates of substitution are very different; Pd(II) complexes are 10^3–10^5 more reactive than Pt(II) complexes [1,23–25]. *cis*-Pd(II) complexes, the analogues of cisplatin (and its subsequent generational drugs) have not been as much successful anti-tumour drugs as the latter due to serious side effects caused by rapid hydrolysis of their leaving groups in the cytoplasm, producing highly reactive species which never reach the targeted DNA because of their facile deactivation by bio-nucleophiles [12,26]. *cis*-Pd(II) complexes are also rapidly isomerised into their *trans* isomers [26–28]. For instance, *cis*-[Pd(NH₃)₂Cl₂] and *cis*-[Pd(DACH)Cl₂], (DACH: (1*R*,2*R*)-(−)-1,2-diamine-cyclohexane) are both inactive against most tumours due to the fast *in vivo* hydrolysis and coupled inactivation reactions. In addition, [Pd(NH₃)₂Cl₂] undergoes facile isomerisation to its equally inactive *trans*-conformation [22,29]. One strategy to circumvent this, is to design Pd(II) complexes that are less prone to deactivation by bio-nucleophiles. This can be achieved through coordination of spectator ligands which lower the electrophilicity of the metal centre through π/σ-donation or use of ligands that are bulky or have significant steric hindrance to the approach of nucleophiles, particularly in the *cis* positions of the Pd(II) complexes. The ligands should preferably be multidentates to guarantee thermodynamic stability of the complexes through the chelate effect [26,30]. Good candidates are ligands such as the (N/S)ˆ(N/C)ˆ(N/S) type, C = phenyl, N/S = heterocyclic aromatic rings. The electronic and steric effect of such spectator ligands can potentially modulate the rate of deactivation of their Pd(II) complexes caused by the ubiquitous bio-nucleophiles. The formation of highly reactive species *in vivo* can be reduced if sterically-hindered ligands particularly in the *cis*-positions of Pd(II) complexes are used. Such structural modification aim at kinetically or thermodynamically stabilizing the candidate Pd(II) complexes, bears the hope for an improved cytotoxic effect against cancer cells through a kinetic deceleration effect [3,4,31,32].

Pd(II) or Pt(II) complexes coordinated with the terpyridine (terpy) ligand or its derivatives are highly reactive [33,34–37]. Due to the high conjugation of the terpy ligand, it accepts electron density through its low-lying π* molecular orbitals from the metal-centred orbitals, leading to the stabilization of the five-coordinate intermediate during a substitution process [38,39]. Comparative reactivity data has demonstrated that extending the π-conjugation of a terpy-type ligand by fusing additional aromatic rings generally enhanced π-back bonding, leading to higher reactivity. For example, when the terpy structure was modified to 2-(2′-pyridyl)-1,10-phenanthroline [40] the rate was doubled. However, the presence of substituents at the 4′-position of the terpy ligand [40,41] and electron donating groups at the 4, 4′ and 4″ positions lowered the rate of substitution by diminishing the extent to which electron density is π-back donated into the terpy ligand [41–43].

Modification of the terpy's flanking (lateral or terminal) rings with other aromatic groups has potential to have a profound influence on the reactivity of the complexes. Bulky aromatic rings are likely to slow down the rate of substitution regardless of their σ/π-donor character. Comparative rate data for [Pt(II)(NˆNˆN/NˆCˆN)Cl]ⁿ, NˆNˆN/NˆCˆN = tridentate of a terpy ligand framework; *n* = 0; 1, showed that chloride substitution rate was significantly reduced when the two *cis*-pyridyl rings of terpy were replaced with *N*-pyrazol-2-yl groups [44,45]. The *cis*-coordinated *N*-pyrazol-2-yl lateral rings σ/π-donated electrons from its pyrazollic-N donor atoms to orbitals of appropriate symmetry on the metal centre [44,45]. However, the effect on the rate of substitution of coordinated tridentates, incorporating *cis*-positioned *N*-pyrazol-2-yl groups on the [Pd(II)(2,6-bis(substituted-/*N*-pyrazol-2-yl)pyridine)Cl]⁺ complexes has not been studied. Given the good π/σ-donor properties of the *N*-pyrazol-2-yl group and the anticipated hope of lowering down the substitution reactivity of the Pd(II) complexes, the role of *cis*-coordinated *N*-pyrazol-2-yl groups on the rate of chloride substitution from four Pd(II) complexes, **PdL1**–**4** (whose structures are shown in Fig. 1) was studied.

Density function theory (DFT) was used to optimise the ground state structures of the complexes and relevant data was used to support the observed reactivity trends. The single X-ray crystal structures of **PdL2**, **PdL3** and **PdL4** are also reported.

To probe on the non-covalent/covalent interactions of complexes, **PdL1**–**4** with DNA, the complexes were spectrophotometrically titrated with a CT-DNA or an EtBr/CT-DNA (EtBr = 3,8-diamino-5-ethyl-6-phenylphenanthridinium bromide and CT-DNA = calf thymus DNA) fluorescent probe soluteion. Furthermore, *in vitro* anticancer activity of the complexes, **PdL1**–**4** was evaluated by the colorimetric MTT [3-(4,5-dimethylthiazol-2-yl)-2,5-diphenyltetrazolium bromide] assay while nucleus morphological changes were evaluated by the acridine orange/EtBr (AO/EtBr) fluorescence staining assay method.

2. Experimental section

2.1. Materials and procedures

All syntheses were performed under nitrogen atmosphere using standard Schlenk line techniques. All chemical reagents and solvents were procured from Sigma-Aldrich and used as supplied. The NˆNˆN ligands: Terpy, **L1**, was procured from Sigma Aldrich, while 2,6-bis(*N*-pyrazol-2-yl) pyridine [46] **L2**; 2,6-bis (3,5-dmethyl- *N*-pyrazol-2-yl) pyridine [46,47] **L3** and 2,6-bis(3,5-dimethyl-N-pyrazol-2-ylmethyl) pyridine [46,48] **L4**, were synthesized according to the standard literature methods with minor modifications as described in the Notes NSI 1, in the Electronic Suppementary Information (ESI) and characterized.

2.2. Preparation of complexes

2.2.1. [Chlorido(2,2′:6′,2″-terpyridine)Pd(II)]Cl (PdL1)

This complex was prepared by a modified procedures [49]. K₂PdCl₄, (0.163 g, 0.5 mmol) was dissolved in 30 mL of deionized water and filtered into a reaction flask. A 2,2′:6′,2″-terpyridine (terpy) solution which had been prepared by dissolving 0.1165 g (0.5 mmol) in 20 mL of

methanol was gradually added to the reaction flask. A light orange precipitate formed immediately. The mixture was digested (*ca.* 50 °C) for 2 h. Thereafter, the volume of solvent was reduced to about 10 mL under vacuum. The solid which formed was filtrated on a Buchner funnel to yield a light orange crystalline precipitate. The precipitate was washed with diethyl ether (3 × 20 mL) and dried at 50 °C under vacuum. Yield 0.1925 g, 86.2%. ^{1}H NMR 400 MHz (CD$_3$OD, ppm): δ = 7.77 (dd, 2H), 8.48–8.44 (m, 4H), 8.37(td, 2H), 7.89(s, 1H), 7.78(d, 2H). ^{13}C NMR (100 MHz CD$_3$OD, ppm): δ = 78.01, 124.1, 124.8, 128.3, 142.2, 142.7, 152.3, 155.2. TOF MS-ES$^+$, *m/z*: 375.9579 [M - Cl]$^+$. *Anal. Calc for* C$_{15}$H$_{11}$N$_3$PdCl$_2$.2H$_2$O: C, 40.34; H, 3.39; N, 9.41. *Found*: C, 40.32; H, 3.30; N, 9.20%.

2.2.2. *[Chlorido(2,6-bis(N-pyrazol-2-yl)pyridine)Pd(II)]Cl (PdL2)*

PdL2 was prepared according to the procedure of Willison and co-workers [50] with some modifications. K$_2$PdCl$_4$ (0.1959 g, 0.60 mmol) was dissolved in 30 mL of deionized water and filtered into a reaction flask. A solution of 2,6-bis(*N*-pyrazol-2-yl)pyridine made by dissolving (0.15 g, 0.71 mmol) in 20 mL of methanol was gradually added to the flask. A tanny-yellowish precipitate was formed immediately. The mixture was refluxed for 2 days at 70 °C. The tanny-yellowish solid was removed by filtration. The filtrate was reduced to near dryness under vacuum and the resultant yellow solid was washed with cold water, methanol, chloroform, diethyl ether and hexanes. (0.1436 g, 56.4%). ^{1}H NMR (400 MHz, CD$_3$OD, ppm): δ = 9.05 (d, 2H), 8.64 (t, 1H), 8.13 (d, 2H), 8.92 (dd, 2H), 6.96 (d, 2H). ^{13}C NMR (100 MHz, CD$_3$OD, ppm): δ = 109.0, 110.6, 133.2, 145.8, 146.5. MS-ES$^+$, *m/z*: 353 [M-Cl]$^+$ *Anal Calc* for C$_{11}$H$_9$N$_5$PdCl$_2$.2H$_2$O: C, 31.12; H, 3.09; N, 16.49 *Found*: C, 31.02; H, 3.00; N, 16.22%. X-ray quality crystals were grown from slow evaporation of a mixture methanol/water solution of **PdL2**.

2.2.3. *[Chlorido(2,6-bis(3,5-dimethyl-N-pyrazol-2-yl)pyridine)Pd(II)]Cl (PdL3)*

The complex was prepared by a procedure analogous to **PdL2**, using 2,6-bis(3,5-dimethyl-*N*-pyrazol-2-yl)pyridine as the ligand. The yellow solid was washed thoroughly with diethyl ether and hexane. (0.142 g, 96.3%). ^{1}H NMR (400 MHz, CD$_3$OD, ppm): δ = 2.63 (s, 6H), 2.86 (s, 6H), 6.52 (s, 2H), 7.88 (t, 2H), 8.49 (t, 1H). ^{13}C NMR (125 MHz, CD$_3$OD, ppm): δ = 12.9, 78.4, 108.5, 113.2, 145.4, 146.6, 147.5, 160.4. MS-ES$^+$ *m/z*: 410 [M - Cl]$^+$. *Anal Calc for* C$_{15}$H$_{17}$N$_5$PdCl$_2$.2.5H$_2$O: C, 36.79; H, 4.53; N, 14.30 *Found*: C, 36.78; H, 4.26; N, 14.05%. X-ray quality crystals were grown from slow diffusion of diethyl ether into methanol solution of **PdL3**.

2.2.4. *[Chlorido(2,6-bis(3,5-dimethyl-N-pyrazol-2-ylmethyl)pyridine)Pd (II)] BF$_4$ (PdL4)*

Modified procedure [51] was used. To a solution of 2,6-Bis(3,5-dimethyl-*N*-pyrazolylmethyl)pyridine (0.1152 g, 0.39 mmol) in CH$_2$Cl$_2$ (20 mL) was added [Pd(CH$_3$NC)$_2$Cl$_2$] (0.1011 g, 0.39 mmol). The solution was stirred for 12 h and the product precipitated by addition of hexane (20 mL) to give a pink solid (0.1546 g, 0.3275 mmol). The solid was then suspended in CH$_2$Cl$_2$ (10 mL) and a solution of NaBF$_4$ (0.036 g, 0.3275 mmol) in CH$_2$Cl$_2$ (10 mL) was added and the mixture stirred for 10 min. The resultant mixture containing Pd black was filtered over Celite to give a clear solution. About 20 mL of hexane was added to the filtrate to induce precipitation. The mixture was kept at −4 °C to afford colourless single crystals suitable for X-ray analysis. (0.0441 g, 25.7%). ^{1}H NMR (400 MHz CD$_3$OD, ppm): δ = 8.20 (t, 1H), 7.90 (d, 2H), 6.13(m, 4H), 5.78 (d, 2H), 2.56 (s, 6H), 2.47 (s, 6H). ^{13}C NMR (100 MHz, CD$_3$OD, ppm): δ = 12.9, 78.4, 108.5, 113.2, 145.4, 146.6, 147.5, 160.4. MS-ES$^+$ *m/z*: 438 [M – BF$_4$]$^+$. *Anal Calc for* C$_{15}$H$_{17}$N$_5$PdClBF$_4$: C, 38.96; H, 4.04; N, 13.36 *Found*: C, 38.64; H, 3.66; N, 12.97%.

2.3. *Physical measurements and instrumentation*

^{1}H NMR and ^{13}C NMR spectral data of ligands and complexes were acquired on a using Bruker Avance DPX 400 NMR or DPX 500 with a 5 mm BBOZ probe at 30 °C. Low-resolution electron-spray ionization (ESI$^+$) data were acquired on Shimadzu LC-MS 2020 or on a Waters TOF Micro-mass LCT Premier spectrometer in a with a positive ion mode. Exemplary NMR and mass spectra for the synthesized ligands and complexes are shown in Figs. SI 1–19, ESI. Elemental compositions of the ligands and complexes were determined using a Thermo Scientific Flash 2000 or a Carlo Erba Elemental Analyzer 1106. A Cary 100 Bio UV–visible spectrophotometer was used to determine the suitable wavelengths for monitoring the substitution reactions. The wavelengths selected for kinetic analysis are reported in Table SI 1, ESI. An applied Photophysics SX 20 stopped-flow reaction analyzer coupled to an online data acquisition system was used to measure the rates of the substitution as a function of concentration and temperature. The instrument was thermo-controlled within ±0.1 °C. The X-ray data was collected on a Bruker Apex Duo fitted with an Incoatec microsource operating at 30 W power and Oxford Instruments Cryojet operating at 100(2) K.

2.4. *Single-crystal X-ray crystallography*

The X-ray data of the complexes **PdL2**–**4** were obtained from a Bruker Apex Duo fitted with an Incoatec microsource operating at 30 W power and Oxford Instruments Cryojet operating at 100(2) K. The data were collected with graphite monochromated Mo Kα (λ = 0.71073 Å) radiation at a crystal-to-detector distance of 50 mm. The structures were solved by direct methods SHELX-2014 [52] and WinGX [53] and refined with full-matrix least-squares technique on F^2 using SHELX-2014 [52]. All hydrogen atoms were included as idealised contributors in the least-squares process.
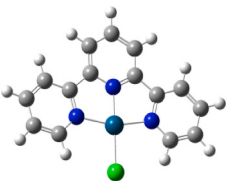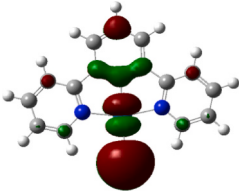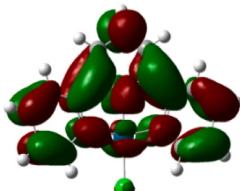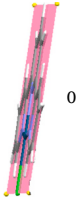
2.5. *Kinetic measurements*
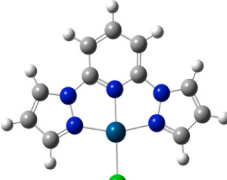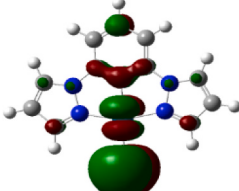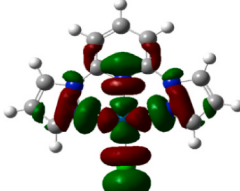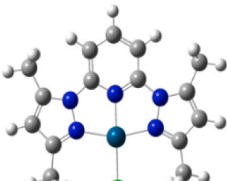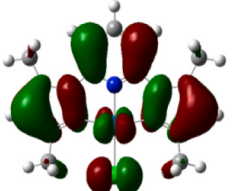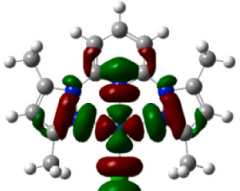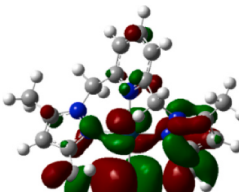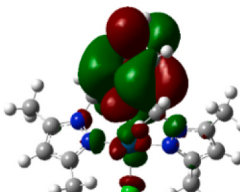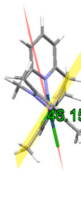
Solutions of complexes, **PdL1**–**4** (3.0 × 10^{-4} M) supplemented with 30 mM lithium chloride (LiCl) were prepared for measuring the rates of substitutions. LiCl was used to prevent any possibility of spontaneous solvolysis of the chloro complexes. The rate of substitution was measured by varying the ligand concentration at 50, 40, 30, 20, and 10-fold excess of the complex concentration. This simplified kinetics to pseudo-first-order. Measurement of the rates of substitution of complexes, **PdL1**–**4** as the [Nu] was varied, were carried out at 298 K except for the reaction of **PdL1** and **Tu**, for which it was carried at 293 K. This reaction was ultrafast, it could not be monitored reliably on the stopped-flow instrument at 298 K. To determine activation parameters, $\Delta H^{\neq}$ and $\Delta S^{\neq}$, rates were measured as a function of temperature within 20 °C to 40 °C with 5 °C intervals for all the substitution reactions except for the reaction of **PdL1** and **Tu**, for which a range of 10 °C to 20 °C with an interval of 2.5 °C were used. The second-order rate constants, k_2, were obtained from slopes of a regressed linear plots of k_{obs} *versus* [Nu] using OriginPro 9.1® software.

2.6. *Computational modelling*

To understand the structure, steric and electronic factors of the complexes which may control the kinetics of the reactions, ground state electronic structures of complexes, **PdL1**–**4** were optimized using the density functional theory (DFT). The DFT calculations were performed with the Gaussian 09 program suite [54] using the B3LYP (Becke 3-Lee-Yang-Parr) functional method, utilizing LANL2DZ (Los Ala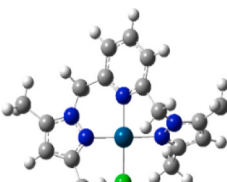mos National Laboratory 2 Double ζ) [55] as the basis set. The influence of solvent was evaluated *via* single-point computations using the C-PCM (conductor-like polarizable continuum model) [56,57] in methanol solvent. All the complexes were modelled with a formal charge of +1 and at singlet state.

Table 1
DFT optimized minimum-energy structures, HOMO and LUMO frontier molecular orbitals, with respective planarity for complexes, **PdL1**–**4** at B3LYP/LANL2DZ level of theory (isovalue = 0.02).

Complex structure	HOMO maps	LUMO maps	Planarity/dihedral angle (°)
PdL1			0
PdL2			0
PdL3			0.71
PdL4			46.15

2.7. DNA-binding experiments

2.7.1. UV–visible absorption titrations of complexes with CT-DNA

DNA titration/binding studies [58] were done to give useful information to help understand the complexes' anticancer mechanism of action in biological systems details of which are described (Notes NSI 2, ESI). A concentration (16 μM) of each Pd(II) complex, (**PdL1**–**4**) dissolved in 2.0% DMSO (because it was established that neither the non-leaving tridentate ligand nor the leaving chlorides of the Pd(II) complexes were displaced by the DMSO solvent) was titrated spectrophotometrically with increasing aliquots of CT-DNA (0–200 μM) prepared in a 5 mM Tris-HCl/50 mM NaCl buffer (pH = 7.2). To eliminate the absorbance of CT-DNA, the requisite amount of CT-DNA were added to both reference and sample solutions. Details on the titration are as previously reported [58–60]. The binding strength (K_b) of Pd(II) complexes were calculated using the Wolfe-Shimer equation [61] (Eq. (S1), ESI) as described in literature [58–60].

2.7.2. Competitive quenching of fluorescence of CT-DNA–EtBr binding studies

The competitive binding of the complexes, **PdL1**–**4** onto the CT-DNA was probed spectrophotometrically by titrating the solution of a fluorescent probe, CT-DNA–EtBr, (EtBr = 3,8-diamino-5-ethyl-6-phenyl-phenanthridinium bromide) with complexes, **PdL1**–**4**. The fluorescent probe solution (comprising 20 μM CT-DNA and 20 μM EtBr as a bound CT-DNA–EtBr complex) was prepared in 5 mM Tris-HCl/50 mM NaCl buffer (pH = 7.2). Aliquot amounts of 5 μM **PdL1**–**4** complexes were added (0–300 μM) to the CT-DNA–EtBr fluorescent probe solution, thoroughly mixed and incubated for 10 min before their fluorescence spectra were acquired within the wavelength range of 520 to 700 nm after excitation at 500 nm. The Stern-Volmer(quenching) constant, K_{sv}, $K_{app.}$ and bimolecular rate constant (k, M^{-1} s^{-1}) for the binding of the **PdL1**–**4** complexes (the quenchers, Q) onto DNA was evaluated using the Stern-Volmer equations (Eq. (S2-2c), ESI) [62] as detailed in literature [58–60].

Analysing the fluorescence quenching data according to the Scatchard equation [63] (Eq. (S3), ESI) the associated binding interaction parameters (K_F, n) were evaluated as detailed in literature [58–60]. To correct for the primary/secondary inner filter effect (IFE) [64] of the fluorescence during the competitive quenching titrations, the absorbance of the CT-DNA was measured at the excitation and emission wavelengths of 510 and 597 nm, respectively using a Shimadzu UV-1800 UV–visible spectrophotometer. The absorbance data was used to correct [59,60] for IFE on the measured fluorescence of the CT-DNA–EtBr probe during its titration with complexes **PdL1**–**4** according to Eq. (S4), in Notes NSI 3, ESI.

Table 2
DFT-calculated parameters for complexes, **PdL1–4**. Bond distances and angles are given in Table 3 (for easier comparison with the X-ray diffraction data).

Property	PdL1	PdL2	PdL3	PdL4
Energy gap (eV)				
LUMO (eV)	−3.307	−3.114	−2.969	−2.286
HOMO (eV)	−7.296	−7.388	−7.286	−6.806
$\Delta E_{LUMO\text{-}HOMO}$	3.989	4.274	4.317	4.520
NBO charges				
Pd^{2+}	0.582	0.582	0.567	0.433
Cl	−0.522	0.489	−0.498	−0.424
Electrophilicity index (ω)	7.08	6.45	6.10	4.57
Dipole moment (Debye)	13.16	15.35	14.82	14.20

2.8. Variation of CT-DNA viscosity with additions of complexes

The viscosity of CT-DNA upon addition of aliquots of complexes **PdL1–4** or EtBr was measured using an Ubbelodhe viscometer with manual timing as previously reported [59,60]. More details are described in Notes NSI 4, ESI. The solution column was totally immersed in a thermostatic water bath maintained at 25 (±0.l) °C.

2.9. In vitro cytotoxicity and morphological studies

The Vero (normal healthy cells) and human breast adenocarcinoma (MCF-7) cell lines were obtained from the National Centre for Cell Sciences Repository, University of Pune, India. The Vero and MCF-7 cells were grown as previously reported [59,60] (more details are found in Notes NSI 5, ESI). The *in vitro* cytotoxicity of complexes, **PdL1–4** against Vero and MCF-7 breast cancer cells was evaluated using the 3-(4,5-dimethylthiazol-2-yl)-2,5-diphenyltetrazolium bromide (MTT) assay [65]. The respective IC_{50} values were determined by nonlinear regression analysis of the % cell viability *versus* concentration of the complexes using OriginPro 9.1®.

The morphological changes/damages caused on the MCF-7 cells by complexes, **PdL1–4** were further investigated by using the AO-EtBr (AO = acridine orange) [66] staining microscopy as previously reported [59,60]. The visual images of the morphological changes on the MCF-7 cells after staining were captured on a FLoid® cell imaging station (Life Technologies).

3. Results and discussion

3.1. Computational details

DFT lowest-energy structures of the complexes, **PdL1–4** were calculated and the data used to explain the observed trend in rates of reaction. The optimized geometry, frontier molecular orbitals and the planarity structures alongside calculated dihedral angles of the complexes are presented in Table 1, whereas the extracts of the calculated

data are presented in Table 2.

The frontier orbital mappings from Table 1 reveal that the HOMO (highest occupied molecular orbital) electron iso-densities are an admixture from Pd's 4d orbitals and Cl's 3p orbitals as well as from the π MOs (molecular orbitals) on the spectator ligand moieties. In the HOMOs of **PdL1** and **PdL2**, the pyridyl moiety is a major contributor. In contrast, pyrazolyl moieties' contribution is evident for the HOMOs of **PdL3** and **PdL4**. The LUMOs (lowest unoccupied molecular orbitals) are however evenly distributed for **PdL2** and **PdL3** except in **PdL1** and **PdL4** where the distribution is concentrated on the pyridyl fragments with minor contributions around the Pd metal centre. Significantly, the LUMO electron iso-density of **PdL1** is centred on the pyridyl rings, has minor features on the Pd and has no contribution from the Cl atom. This is consistent with the fact that terpyridine ligand system is a better π-acceptor than the pyrazolyl moieties as supported by the lowest ΔE value (Table 2) of **PdL1** than the rest of the complexes. A better energy matching between Pd's dπ orbitals and extended π* orbitals of terpy promotes efficient delocalization of electrons compared to the rest of the complexes.

Calculated data in Table 2 illustrate that the complexes adopt slightly distorted square-planar geometry with N5–Pd–N1 deviating from the ideal 180° by 5.5° – 14.5°. On the other hand, the geometry optimized structures of **PdL1** and **PdL2** show the metal atoms lie in the plane of the ligand structures, while in **PdL3** and **PdL4**, the pyrazole fragments are twisted out-of-plane with a dihedral angle of 0.71° and 46.15° respectively, away from N3–Pd–Cl main axis (see Table 1). The large out-of-plane twist in **PdL4** is due to the methylene spacer groups causing fluxional flexibility within the tridentate ligand. This demand is also depicted in the single X-ray diffraction molecular structure of the complex (Fig. 2c).

The energy band gap of the HOMO-LUMO increases in the order **PdL1** < **PdL2** < **PdL3** < **PdL4**, which is also the increasing order of the rate of chloride substitution from the complexes (Table 4). In addition, the monotonic increase in the HOMO energy level from **PdL1** to **PdL4** is an indication that the structural changes in the spectator ligands from **L1** to **L2–4** are accompanied by a stronger donation of electron density into Pd-centred orbitals. The same changes also monotonically increase the LUMO energy, and this cause a reduction in π-acceptability of the ligands in the same order [67].

3.2. X-ray crystal determination of the complexes, PdL2–4

The molecular structures of the complexes **PdL2** ($C_{11}H_9N_5PdCl_2 \cdot 2H_2O$), **PdL3** ($C_{15}H_{17}N_5PdCl_2 \cdot CH_3OH$) and **PdL4** ($C_{17}H_{21}N_5PdClBF_4 \cdot CH_2Cl_2$) were solved by single-crystal X-ray crystal diffraction. The crystallographic data and refinement structural parameters for complexes, **PdL2–4** are summarized in Table 3, while their molecular structures are shown in Fig. 2.

The complexes **PdL2** and **PdL3** crystallise each with a chloride
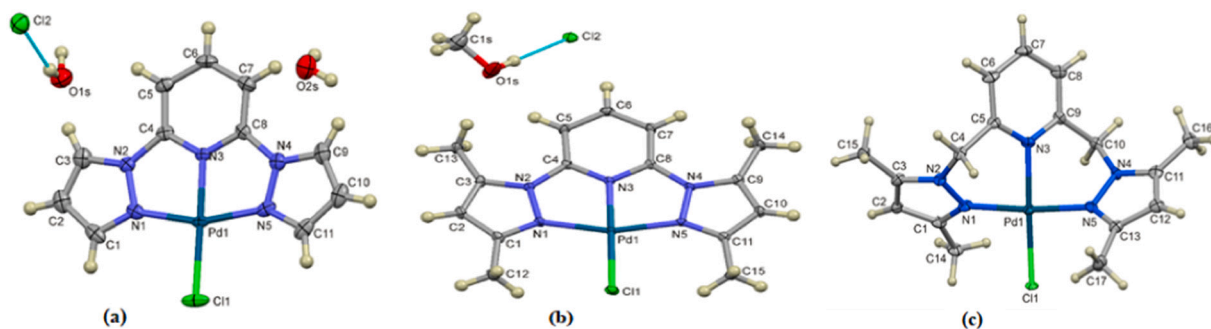
Fig. 2. Molecular structures of **PdL2** (a), **PdL3** (b) and **PdL4** (c) with atom numbering scheme. The displacement ellipsoids of atoms are shown at the 50% probability level. Unconventional hydrogen bonding interactions between the counter Cl⁻ and H atom of water or methanol are shown by a blue dashed line. The counter ion and solvent molecule in *2c* have been omitted for clarity.

Table 3
Crystal data and structure refinement for **PdL2**–**4**.

	PdL2	PdL3	PdL4
Molecular formula	$C_{11}H_9N_5PdCl_2.2H_2O$	$C_{15}H_{17}N_5PdCl_2.CH_3OH$	$C_{17}H_{21}N_5PdClBF_4.CH_2Cl_2$
M_r	424.56	476.68	608.97
Crystal size/mm^3	$0.210 \times 0.190 \times 0.140$	$0.180 \times 0.140 \times 0.110$	$0.36 \times 0.19 \times 0.11$
T/K	100(2)	100(2)	100(2)
λ/Å	0.71073	0.71073	0.71073
Crystal system	Monoclinic	Monoclinic	Triclinic
Space group	$P21/c$	$P21/c$	$P\text{-}1$
a/Å	11.2092(7)	10.2667(4)	7.7353(3)
b/Å	6.7184(4)	11.0524(5)	12.3436(9)
c/Å	20.5656(12)	16.0338(7)	13.4839(9)
α/°	90	90	115.036(3)
β/°	105.340(3)	95.028(2)	90.896(3)
γ/°	90	90	92.142(4)
V/Å^3	1493.57(16)	1812.38(13)	1164.98(14)
Z	4	4	2
D_c/Mg m^{-3}	1.888	1.747	1.736
μ/mm^{-1}	1.611	1.334	1.189
F(000)	840	960	608
θ range/°	1.884–27.168	2.241–28.263	1.668–27.075
Reflections collected (independent)	12,629 (3292)	16,424 (4460)	18,239 (4962)
R_{int}	0.0252	0.0279	0.0587
No. of parameters (restraints)	205 (6)	232 (0)	330 (unknown)
R indices (all data)	$R_1 = 0.0386, wR_2 = 0.0772$	$R_1 = 0.0269, wR_2 = 0.0562$	$R_1 = 0.0807, wR_2 = 0.1518$
Goodness-of-fit on F^2	1.054	1.072	1.034
Max, Min Δρ/e Å^{-3}	1.742, −0.898	0.846, −0.606	1.564, −2.183

counter ion, while **PdL4** crystalizes as a tetraflouroborate salt. In addition, the crystallization of **PdL2** is stabilised by two water solvent molecules while that of **PdL3** and **PdL4** have a methanol and a dichloromethane solvent molecule, respectively.

All the ligands coordinate to the Pd(II) ion tridentately by the N3 of the central pyridyl ring and the N1/5 atoms of the terminal pyrazolyl rings, while the fourth position is covalently bonded to a Cl1 ligand (Fig. 2). The Cl2 (counter ions) of **PdL2** and **PdL3** and BF_4^- for **PdL4** are held by unconventional hydrogen contacts/interactions (indicated by the blue dashed line in Fig. 2a and b) between the hydrogens of one water molecule and methanol molecule for **PdL2** and **PdL3**, respectively. The donor/acceptor distance for the H-bonding, Cl2…H–O1$_{(water)}$ is 3.182(4) Å in **PdL2** while that of Cl2…H–O1$_{(methanol)}$ is 3.044(2) Å for **PdL3**.

The complexes adopt a distorted square-planar coordination geometry around the metal centre given that the angles N1–Pd1–N3, N5–Pd–N3, N3–Pd–Cl1 and N5–Pd–Cl1 deviates approximately by 2° – 10° from the expected square-planar angle of 90°. The bite angle N5–Pd1–N1 also deviates from linearity (180°) to 160.77(11)° 160.33(6)° and 174.1(2)° for **PdL2 PdL3** and **PdL4**, respectively. In addition, N3–Pd1–Cl1 angles are 178.74(8)°, 179.17(5)° and 177.3(1)° for **PdL2**, **PdL3**, and **PdL4**, respectively; they too depict slight deviation from linearity. The bite angles are however comparable to the DFT-calculated values (Table SI 1, ESI). The bond angle N3–Pd1–Cl1 for **PdL2** is comparable to 178.91(13)° reported for an X-ray structure of an analogous Pt(II) complex [50], while that of **PdL4** (177.3(1)°) is almost equal to 177.63(12)° of analogous X-ray structure, [chlorido(2,6-bis(3,5-dimethyl-N-pyrazol-2-ylmethyl)pyridine)Pd(II)]BAr$_4$, (Ar = 3,5-(CF$_3$)$_2$C$_6$H$_3$) [51]. The difference between the two being that the latter crystallized with a bulky counter ion. Selected bond lengths/distances and angles of the X-ray structures of **PdL2**–**4** are tabulated in Table SI 1, ESI. Also in the same table, theoretical DFT calculated values are included for comparison purposes.

The bond distances N3–Pd1 of 1.938(2) Å (for **PdL2**) and 1.941(2) Å (for **PdL3**) are shorter than the Pd1–N1 or Pd1–N5 distances. In **PdL4**, the N3–Pd1 distance is longer (2.204(4) Å) than in the former two complexes, reflecting the weakening of the *trans* bond, possibly to the out-of-plane-twisting of **L4** as dictated by the steric demands of the two methyl substituents on its terminal N-pyrazol-2-yl moieties. Overall, the range of bond distances are comparable and within the ranges reported

for other X-ray related structures [50,51,68].

For all the three complexes, the Pd1–N3 bond distances are noticeably shorter than the Pd1–Cl1 being 2.273(1) Å; 2.297(1) Å and 2.311(1) Å for **PdL2**, **PdL3**, and **PdL4**, respectively. Changes in the structures of coordinated ligands **L2**-**L4** are accompanied by the strengthening of the Pd—N3 bond. The DFT data (simulated solvent medium) is in good agreement with the solid state X-ray diffraction data, with the former value being higher (<5% RSD) than the latter.

PdL2 and **PdL3** stack as slip-up and head-to-head inversion dimers along the c axis. The Pd—Pd distances between the dimers are 3.3622(3) Å (for **PdL2**) and 3.4697(3) Å (for **PdL3**) (see Fig. SI 20, ESI) and are shorter than 4 Å, the minimum bond distance for effective $(4d_{z}^2)$–Pd$^i(4d_{z}^2)$ overlap to enable metal-metal-to-ligand charge transfer (MMLCT) in the solid state. These intermolecular metal–metal interactions have been observed in the supramolecular structures of Pt(II) complexes with similar ligand structures [50]. In sharp contrast to the supramolecular structure of the former two complexes, **PdL4** molecules do not crystalize as dimeric cations; the Pd–Pd^i distance of **PdL4** (10.1507(9) Å) is much greater than the 4 Å minimum threshold for metal-metal interactions in d^8 metal complexes. This is probably due to the twisted conformation of the *cis*-coordinated N-pyrazol-2-yl forced by the steric demands of their bis(3,5-dimethyl) substituents on the packing of **PdL4** cations in the solid structure, see Fig. 2c. In addition, the solid structure of **PdL2** has a C–H⋯Cl1 bonding linkage indicating intermolecular interaction as shown in Fig. SI 21, ESI, which is not the case with **PdL3** and **PdL4** complexes.

3.3. Kinetic and mechanistic studies

The rate of substitution of chloride ligands from complexes, **PdL1**–**4** was studied as a function of nucleophile concentration and temperature using thiourea nucleophiles *viz.*, **Tu**, **Dmtu** and **Tmtu** under *pseudo* first-order conditions. Rates were monitored on the stopped-flow spectrophotometer. The optimal wavelengths at which each reaction could be monitored were determined spectrophotometrically by recording the UV/Vis-spectral changes before and after mixing the complex and the nucleophile. Typical spectral changes recorded soon after mixing the reactants are shown in Fig. SI 22, ESI, for a trial reaction of **PdL3** and **Tmtu**. The wavelengths for monitoring the reactions of complexes, **PdL1**–**4** and the nucleophiles are presented in Table SI 2, ESI.
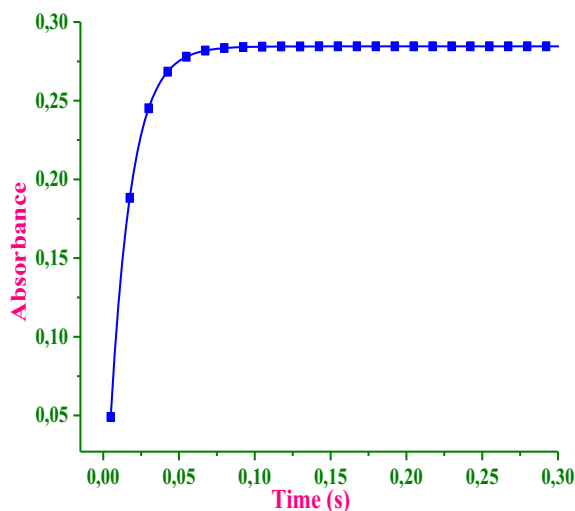
Fig. 3. Real-time absorbance data for the reaction of **PdL2** and **Dmtu** at 298 K recorded at 380 nm on a stopped-flow analyzer.
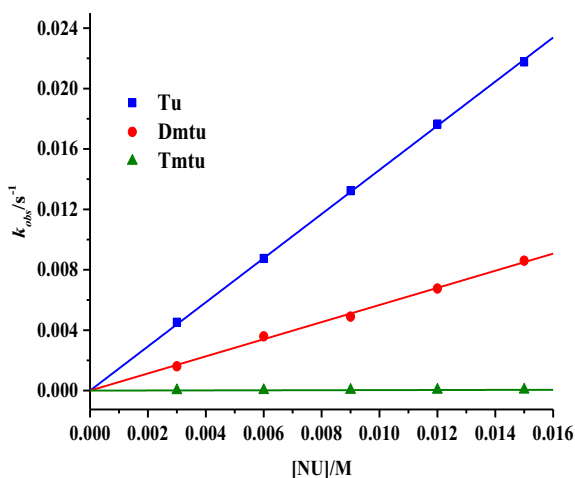

Fig. 4. Plots of the k_{obs} *versus* [Nu] for chloride substitution from **PdL4** by the thiourea nucleophiles at T = 298 K and I = 30 mmol LiCl.

The real time changes in absorbance accompanying the reaction of **PdL2** and **Dmtu** at 298 K and wavelength 380 nm recorded by mixing is shown in Fig. 3.

As shown in Fig. 3, there is a good least-square fit of data to a generic single-exponential standard Eq. (1).

$$A_{\mathrm{t}} = A_{\mathrm{o}} + (A_{\mathrm{o}} - A_{\alpha})e^{(-kobs\ t)} \tag{1}$$

where A_{t}, A_{o} and A_{α} represent the absorbance of initial reaction mixture, at time t, and at the end of the reaction respectively. The rate data for reactions of other complexes and nucleophiles also fitted perfectly to Eq. (1). The fit generated pseudo-first-order rate constants ($k_{obs.}$). Thus, the substitution reactions are first-order in concentration of both the thiourea nucleophiles and Pd(II) complexes. When the average $k_{obs.}$, were plotted against [Nu] using Origin Pro 9.1®, straight lines with zero intercepts were obtained as shown in Fig. 4 for reactions of **PdL4**. Similar plots for the other complexes are shown in Figs. SI 23–25, ESI, while the values of k_{obs} at each nucleophile concentration are tabulated in Tables SI 3–6, ESI.

Thus, k_{obs} varies linearly with [Nu] as expressed in the rate law: k_{obs} = k_2[Nu]; the substituting thiourea nucleophiles irreversibly displaced the chloride co-ligand from complexes, **PdL1–4**. The rate constants, k_2

Table 4

Rate constants and thermodynamic parameters for reactions of **PdL1–4** complexes and nucleophiles at 298 K.

Complex	Nucleophile	k_2/M^{-1} s^{-1}	$\Delta H^{\neq}$/kJ mol^{-1}	$\Delta S^{\neq}$/J K^{-1} mol^{-1}	Pt(II) k_2/ M^{-1} s^{-1}
PdL1	Tu*	$(1.18 \pm 0.02) \times 10^5$	18 ± 1	-88 ± 4	1494 ± 10[a]
	Dmtu	$(4.1 \pm 0.3) \times 10^4$	23 ± 2	-80 ± 6	448 ± 10[a]
	Tmtu	$(4.66 \pm 0.02) \times 10^3$	49 ± 1	-11 ± 3	82 ± 4[a]
PdL2	Tu	$(1.26 \pm 0.03) \times 10^4$	24 ± 1	-85 ± 3	0.86 ± 0.01[b]
	Dmtu	$(4.99 \pm 0.03) \times 10^3$	32 ± 1	-68 ± 3	0.37 ± 0.01[b]
	Tmtu	$(3.04 \pm 0.09) \times 10^2$	44 ± 1	-86 ± 3	0.17 ± 0.03[b]
PdL3	Tu	$(1.01 \pm 0.01) \times 10^4$	24 ± 1	-87 ± 3	0.31 ± 0.02[b]
	Dmtu	$(4.33 \pm 0.03) \times 10^3$	24 ± 1	-95 ± 5	0.13 ± 0.01[b]
	Tmtu	$(1.13 \pm 0.02) \times 10^2$	63 ± 1	-36 ± 3	0.014 ± 0.001[b]
PdL4	Tu	1.46 ± 0.01	52 ± 2	-67 ± 6	–
	Dmtu	$(5.67 \pm 0.07) \times 10^{-1}$	39 ± 1	-119 ± 4	–
	Tmtu	$(3.28 \pm 0.01) \times 10^{-3}$	61 ± 2	-85 ± 7	–

* $k_{2(298\ \mathrm{K})}$ was extrapolated using linear equation from the Erying plot [ln(k_2/ T) = m($1/T$) + c] from 20 °C to 25 °C assuming the linearity exists up to 25 °C, where $k_{2(293\ \mathrm{K})}$ was measured to be $(1.1 \pm 0.1) \times 10^5$.
[a] Data from ref. [36].
[b] Data from ref. [45].
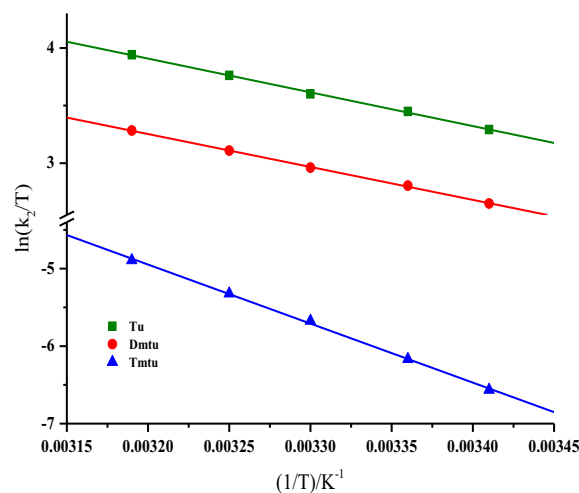
Fig. 5. Eyring plots for the reactions of **PdL3** and nucleophiles.

obtained from the gradient of the linear plots of k_{obs} against [Nu] are summarized in Table 4. Also included in Table 4 for comparison purposes are the k_2 values for the analogous Pt(II) complexes with the same ligand framework found in literature [45]. The rate of chloride substitution by **Tu** from **PdL1** was too fast to be followed reliably at 298 K, therefore it was monitored at 293 K. The k_2 values at 298 K was extrapolated from k_2 value measured at 293 K [$(1.1 \pm 0.1) \times 10^5$ M^{-1} s^{-1}] using an Eyring Free linear relationship of the form: ln(k_2/T) = m $(1/T)$ + c (the relationship is shown in Fig. SI 26 and the extrapolation shown in Fig. SI 27, ESI).

The thermal effect on the rate of substitution was studied within the range of 20 °C to 40 °C with 5 °C intervals for all the substitution

reactions except for **PdL1** and **Tu** for which a range of 10 °C to 20 °C with an interval of 2.5 °C were used. The activation enthalpies ($\Delta H^{\neq}$) and activation entropies ($\Delta S^{\neq}$) were calculated from Eyring plots and values are presented in Table 4. Representative Eyring plots for the rate data of **PdL3** are shown in Fig. 5; similar plots for the reactions of other complexes are shown in Figs. SI 28–30, while the values of $\ln(k_2/T)$ and $1/T$ are tabulated in Tables SI 7–10, ESI.

Comparing the rate constants (Table 4) for the chloride substitution from complexes, **PdL1**–4 complexes by the thiourea nucleophiles, **PdL1** is the most reactive. This is because terpy is a strong π-acceptor ligand due to its highly conjugated and planar ligand framework, the chloride co-ligand in **PdL1** is rapidly substituted by incoming thiourea nucleophiles. The stronger π- acceptor of terpy ensures effective and efficient π-back donation of electrons from the metal d-orbitals into its extended π*-molecular orbitals of the in-plane aromatic pyridyl rings [69–71]. The electrophilicity of the metal centre is increased, making it more positive, hence more prone to nucleophilic attack by the incoming ligands. The increase in the electrophilicity of the Pd(II) ion in **PdL1** is mirrored in the relative magnitudes of the DFT-calculated electrophilicity indices of the **PdL1**–4 complexes (Table 2) which decrease in the order 7.046 (**PdL1**) > 6.451 (**PdL2**) > 6.090 (**PdL3**) > 4.572 (**PdL4**). The high reactivity of Pd/Pt$^{(II)}$(terpy)Cl/H_2O complexes in aqua, aprotic or ionic media, with various nucleophiles is well documented [34–36,69]. Substitution rate constants as high as $(7.8 \pm 0.2) \times 10^5$ M^{-1} s^{-1} at 25 °C for chloro substitution from Pd$^{(II)}$(terpy)Cl by **Tu** have been reported [34].

Using the rate of reaction of **PdL1** with **Tu** as a reference for comparison, the order of the chloride substitution from **PdL1**–4 is **PdL1** > **PdL2** > **PdL3** ≫ **PdL4**. The same trend was also observed for the other two nucleophiles (Table 4). The structure of **PdL2** differs from that of **PdL1** by having two *cis*-coordinated *N*-pyrazol-2-yl rings in place of the pyridyl rings of terpy. Based on the reactions of **Tu**, this difference causes a 10 times decrease in the rate of substitution from **PdL2** compared to **PdL1**. This is so, despite the two complexes sharing common 5-membered rigid and aromatic chelate ligands around their metal ions. As a result, the two complexes have extended and delocalized π-molecular orbitals that efficiently stabilize the metal centre through π-back bonding. It is then logical to make a proposition that the two *cis*-coordinated *N*-pyrazol-2-yl rings of **L2** are significantly weaker π-acceptors of electron density than the pyridyl rings of terpy and thus have a net σ/π donation towards the Pd metal centre. Absorption data profiles of complexes of ruthenium [72,73] coordinated to **L1** and **L2** ligands showed higher energetic metal ligand charge transfer bands (MLCT) in complexes having **L2** ligands than those of **L1** ligands [45,72,73]. The latter class of complexes has a wider energy band gap and thus absorbs at a higher-energy MLCT than the former [45,72,73]. The two laterally coordinated **L2** ligand raises the LUMO of the complex more than it destabilises the HOMO, leading to higher energy MLCT bands. The MLCT difference between the complexes is due to large energy difference (ΔE) between the LUMOs and HOMOs which makes **L2** a poor π-acceptor of electron density than **L1**. In fact they have a poor net σ/π donation towards the Ruthenium metal centre. The same trend and arguments have been reported and put forward for Pt(II) complexes [50] stabilised by the two aforementioned ligands.

The more stabilised π* LUMOs of lateral pyridine rings in **PdL1** readily accepts π-back donation from the metal, as already mentioned, as opposed to two lateral pyrazolyl ring of **L2** that has pyrazollic N atoms making them a better π-donor [74,75] towards the Pd metal centre in **PdL2**. The net poor π-acceptor capacity of the *cis*- coordinated *N*-pyrazol-2-yl rings of **PdL2** is through the pyrazollic-N π-donor atoms. This leads to a build-up of electron density towards the metal centre along the two *cis* Pd-N$_{pyrazollic}$ bonds through π-resonance [44,76], lowering the electrophilicity of the complex and thus retarding the nucleophilic attack by incoming nucleophiles. This is reflected in the relative magnitudes of their electrophilicity indices which decrease in the order: 7.046 (**PdL1**) > 6.451 (**PdL2**), see Table 2. The same effect also raise the

LUMO energy in **PdL2** to −3.114 eV compared to **PdL1**'s − 3.307 eV. Consequently, the HOMO-LUMO energy gap of **PdL2** (4.274 eV) is higher compared to that of **PdL1** (3.989 eV). The pyrazollic-N π-donor effect is enhanced in **PdL3** whose reactivity is further reduced. This is because the two methyl substituents donate electrons into the pyrazole rings which in turn make σ/π-donation towards Pd metal centre, causing its metal centre to be much less electrophilic than **PdL2**'s. The rate of substitution is further reduced as observed experimentally. The relative sizes of the calculated NBO charges of Pd support the observed reactivity trend (Table 2). In addition, it is worth noting that in **PdL2** and **PdL3** the π-backbonding on the *trans*-pyridyl ring competes with the π/σ-donation ability of the *cis*-pyrazolyl rings for the palladium metal centre. The stronger π/σ-donation of the pyrazole reduces the π-backbonding.

When the reactivity of **PdL4** is compared with those of **PdL2**/**PdL3** and **PdL1**, a significant reduction in the rate of substitution by factors which are about 4–5 times (for reactions of **Tu**) is noted. While the steric demands in the flanking bis(3,5-dimethyl-*N*-pyrazol-2-yl) rings of **L3** and **L4** are the same, the two ligands differ in the aromaticity and conformational flexibility of their coordination chelates around the Pd (II). The two methylenic groups bridging the central pyridyl ring and the flanking pyrazole rings introduce flexibility in the two six-membered chelates of **PdL4**. It also destroys the chelate aromaticity of the coordinated ligand, thus isolating each of the donor aromatic rings of **L4**. This prevents electron delocalisation as evident from the aromatic chelates of **PdL3** or **PdL2**. Thus, the π-acceptor property is weakest for **L4**. This causes lowest rates of chloride substitution from **PdL4**. The more flexible six-membered ring chelates of **PdL4** also allow for an out-of-plane coordination twist of **L4**, as depicted in its X-ray crystal structure (Fig. 2c). Deviations of atoms of the coordinated ligand framework from the square-plane containing the Pd atom is largest for **PdL4** and this is also depicted from the side-view of the DFT-optimized structures in Table 1. The chelate rings of **PdL4** have a marked degree of out-of-plane fluxional flexibility. This manifest as aerial hindrance to incoming nucleophiles during a nucleophilic substitution reaction, resulting in reduced rates. A similar effect was reported for the rate of substitution from [Pd(tpdm)Cl]$^+$ (tpdm = tri(pyridine)dimethane) [10,77]. The fluxional movements of the bridging methylene groups of tpdm forced the bridged pyridyl rings of tpdm to be out-of-plane with the metal centre, which significantly introduced steric effects to the incoming nucleophiles. These steric effects retarded the rate of chloride substitution as also observed for **PdL4** in this study.

The reactivity of the complexes, **PdL1**–3 was compared with their analogous Pt(II) complexes [36,45] and the k_2 data is included in Table 4. The chloride substitution from the **PdL1**–3 complexes is about 10^2–10^5 times faster than from their Pt(II) analogues. Pd(II) complexes are more reactive because they form relatively weaker bonds with most donor atoms of labile ligands (OH_2; X = Cl, F$^-$, Br$^-$; N *etc*.) compared to Pt. Moreover, the Pt(II) ion is 'softer' than Pd(II) and therefore is more sensitive to electronic 'communication' with its spectator ligands, particularly the strong π-acceptors [25,69,78,79]. In principle and if need be, it is convenient to increase the reactivity of Pt(II) complexes to match those of their closely related Pd(II) counterparts by varying the electronic properties, whereas reducing the lability of Pd(II) complexes to match their closely related Pt(II) analogues can conversely be achieved through controlling the steric hindrance or bulk of the spectator ligands, more so in their *cis*-positions [10,25,79]. In this study, a combination of electronic and steric factors decreased the reactivity of Pd(II) metal center to match the range reported for Pt(II) complexes with similar structure.

Over all, the rate determining step is bimolecular as evidenced from the low activation enthalpies ($\Delta H^{\neq}$) and negative activation entropy ($\Delta S^{\neq}$) values. The substitution of the chloride from the complexes, **PdL1**–4 by the nucleophiles is associatively activated. In addition to this, rate is sensitive to the steric bulk of the incoming nucleophiles. The nucleophilic order of substituting the chloride ligand from the **PdL1**–4 complexes is **Tu** > **Dmtu** > **Tmtu**, and is a reflection of the increasing
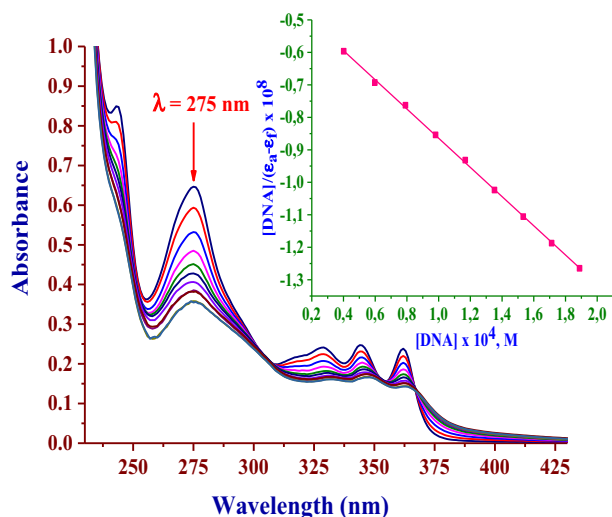
Fig. 6. Absorption spectra of **PdL3** (16 μM) in Tris-HCl/50 mM buffer at pH 7.2 upon addition of CT-DNA (0–200 μM). The arrow shows the change in absorbance upon increasing the CT-DNA concentration. Inset: plot of [CT-DNA] *versus* [DNA]/(ε_a- ε_f) for estimating the binding constant, K_b.

Table 5

The binding constants, quenching constants, and quenching rate constant for interactions of complexes, **PdL1**–**4** with CT-DNA.

Complex	UV titration	Fluorescence quenching parameters: titration of CT-DNA–EtBr by **PdL1**–**4**				
	K_b, M^{-1} (10^4)	K_{sv}, M^{-1} (10^3)	K_{app}, M^{-1} (10^5)	k_q, M^{-1} s^{-1} (10^{11})	K_F, M^{-1} (10^4)	N
PdL1	9.9 ± 0.2	42.0 ± 0.1	22.2 ± 0.2	18.3 ± 0.4	22.3 ± 0.2	1.01 ± 0.05
PdL2	2.7 ± 0.1	4.9 ± 0.1	2.2 ± 0.1	2.2 ± 0.2	1.3 ± 0.1	1.00 ± 0.07
PdL3	1.0 ± 0.1	2.8 ± 0.1	1.6 ± 0.1	1.2 ± 0.1	1.7 ± 0.1	1.00 ± 0.04
PdL4	0.78 ± 0.04	0.99 ± 0.03	0.86 ± 0.05	0.37 ± 0.09	0.15 ± 0.03	1.0 ± 0.05

order of their bulk size and accessibility of their S-donor atoms for nucleophilic attack onto the Pd(II) ions of complexes, **PdL1**–**4**.

3.4. Interactions of the complexes with CT-DNA

3.4.1. Attenuation of the UV–visible absorption of CT-DNA by complexes, PdL1–4

Additions of CT-DNA to complexes **PdL1**–**4** caused a hypochromism in the absorbance of ligand-centred band range from 270 nm to 320 nm. Typical spectral changes accompanying the titrations are given in Fig. 6 for the titration of **PdL3** with CT-DNA; similar graphs are given as Figs. SI 31–32, ESI, for titrations of **PdL1**–**2** and **PdL4** complexes, respectively. The isosbestic points signify inter-conversion between the Pd(II) complexes and the DNA coordinated adducts. Preferential coordinative interactions have been reported for Pd(II) interaction with G4 tetramers of duplex DNA [80]. The binding constants, K_b, for these associative interactions were calculated from the ratio of the slopes to intercepts of the Wolfe-Shimer plots [61] (Eq. (S1), insets to Figs. SI 31–33, ESI). They are presented in Table 5. The moderately high K_b (10^4 M^{-1}) clearly suggest that the complexes, **PdL1**–**4** rapidly coordinate to CT-DNA possibly after some non-covalent pre-associative interactions that includes electrostatic, $\pi-$/hydrogen bonding and weak van der Waal intermolecular forces. Thus, the likely mode of binding is covalent linking *via* groove binding as also corroborated by data from the

viscosity measurements (*vide infra*).

3.4.2. Quenching of CT-DNA–EtBr fluorescence studies

Titration of the highly fluorescent CT-DNA–EtBr solution with complexes, **PdL1**–**4** quenched the emission of the former. The λ_{max} are also shifted slightly to longer wavelengths with each addition as shown in Fig. 7. Analogous graphs are given as Figs. SI 34–36, ESI. By quenching the fluorescence of the CT-DNA–EtBr solution, this is direct evidence that complexes, **PdL1**–**4** competitively displace intercalated EtBr from the DNA base pairs. Typical fluorescence quenching spectral changes are given in in Fig. 7 for the titration of **PdL1**. Linear fitting of spectral data to the Stern-Volmer equation [62] (Eq. (S2), ESI) and Scatchard equation [63] (Eq. (S3), ESI) are given as insets (7a & 7b) to the figure. For quenching data and similar plots for titrations of **PdL2**–**4**, refer to Figs. SI 34–36 and their insets a & b, ESI, respectively. The plots were used to calculate several quenching constants, kinetic and stoichiometric parameters for the binding process and data is given in Table 5. The magnitude of quenching constant, K_{sv} (~10^3 M^{-1}), suggest moderate to strong CT-DNA–**PdL1**–**4** interactions only possible through competitive displacement of EtBr off the DNA base pairs. This occurs possibly through a stabilizing partial insertion of their ligand framework of the complexes into the base pairs with the grooves of CT-DNA followed by rapid coordinative binding to the N7 atoms of guinine bases within the neighbourhood. The range of magnitude of the apparent binding constants (K_{app}), (~10^5 M^{-1}) is however less by two orders of magnitude compared to values (~10^7 M^{-1}) for classical intercalators and metallointercalators [81].

The planar and positive charge of **PdL1**–**4** promotes this concomitant partial insertion and electrostatically interactions with the negative backbone of DNA, before the subsequent coordination of the N7 atoms of the bases onto the complexes. DNA groove binding of **PdL1**–**4** is also supported by the observed trend in viscosity of titrated CT-DNA (*vide infra*). The magnitudes of bimolecular quenching rate constants, k_q for the binding process (Table 5) fall in the 10^{11} M^{-1} s^{-1} range and allude to ultra-fast kinetics. This is typical of the kinetics of non-covalent bimolecular physical and pre-associative interactions between two attractive species. The k_q values are even higher than those reported for typical bio-organic fluorescence quenchers (2.0 × 10^{10} M^{-1} s^{-1}) [59]. Thus, it can be deduced also that EtBr is exchanged or displaced from the CT-DNA statically rather than dynamically.

The magnitudes of the K_F values (10^4 M^{-1}) are moderate, reaffirming the moderate-to-strong binding abilities of complexes, **PdL1**–**4** onto CT-DNA. Overall, the decreasing order of strength of their binding is **PdL1** > **PdL2** > **PdL3** > **PdL4**. This trend is the same as what was observed from the UV–Vis absorption titrations of the complexes with CT-DNA. In addition, the observed binding trend of the complexes is similar to that observed for the rate of substitution of the labile chloride from the complexes (Table 4).

3.4.3. Viscosity of DNA solutions titrated with variable amounts of complexes

Addition of variable concentration (0–12.0 mM) of **PdL1**–**4** to a 50 μM CT-DNA solution (in 5.0 mM Tris-HCl buffer, pH 7.2) did not significantly change the relative viscosity of the solutions, see Fig. 8. In contrast, when the titrant was changed to EtBr (a classical intercalator), the viscosity of CT-DNA solutions increased dramatically (refer to Fig. 8). Based on the marked dissimilarity in the effect on DNA viscosity of complexes, **PdL1**–**4** and a known DNA base-pairs intercalator, it seems reasonable that the associative interaction probed by UV–visible/fluorescent quenching experiments are not purely intercalative in nature. Likely, complexes **PdL1**–**4** interact with DNA by groove binding. However, partial but not full base-pair penetration of the complexes may occur within the groove neighbourhood, thus accounting for why the viscosity of DNA remains almost constant on each addition. Titration of CT-DNA with distamycin [82], (a non-electrostatic DNA groove binder) has a similar viscosity effect to that of the titration with complexes,
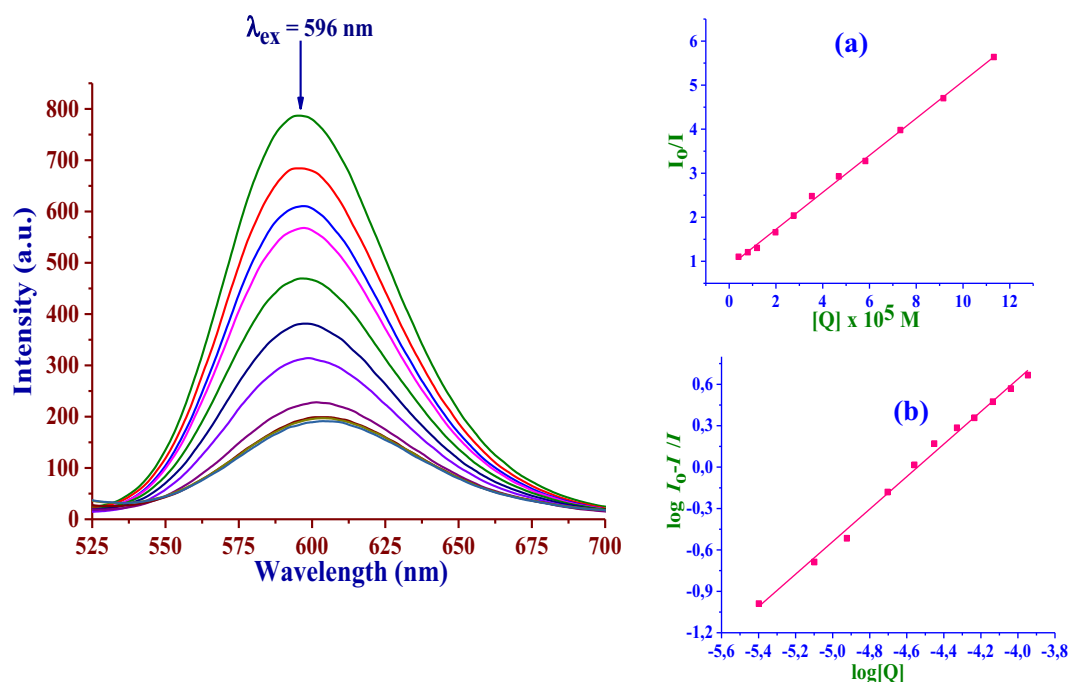
Fig. 7. Fluorescence emission spectra of CT-DNA–EtBr upon titration with Q (the quencher = **PdL1**); [EtBr] = 20 μM; [CT-DNA] = 20 μM and [**PdL1**] range = 0–300 μM. The arrow shows the intensity changes upon increasing [**PdL1**]. (a): Stern-Volmer plot: I_o/I *versus* [Q] and (b): Scatchard plot: $\log[(I_o–I)/I]$ *versus* $\log[Q]$.
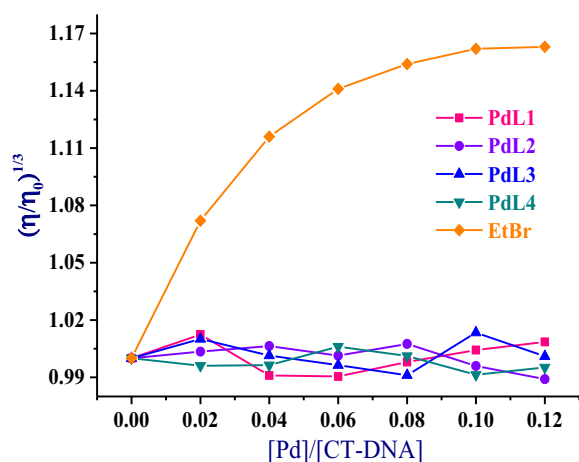

Fig. 8. Relative viscosities of 50 μM CT-DNA in 5.0 mM Tris-HCl buffer, pH 7.2 on addition of variable concentration of complexes, [**PdL1**–**4**] or [EtBr] = (0–12.0 mM).

PdL1–**4**. Thus, these complexes are involved in pre-associative hydrophobic interactions between their tridentate ligands and the hydrophobic groups within the grooves of CT-DNA which leads to their direct covalent linking to the DNA base pairs. This also synergised by electrostatic interactions between the positive charge of the **PdL1**–**4** and the negative backbone of the DNA.

3.5. In vitro cytotoxicity against normal Vero and MCF7 breast cancer cells

3.5.1. Viability of MCF7 cells treated with complexes by the MTT assay

The *In vitro* cytotoxicity of the complexes was evaluated against normal Vero and MCF7 cell lines using the MTT assay. Details are as previously reported [59,60]. The percentage of MCF7 viable cells after treatment of the respective **PdL1**–**4** at variable concentrations are given
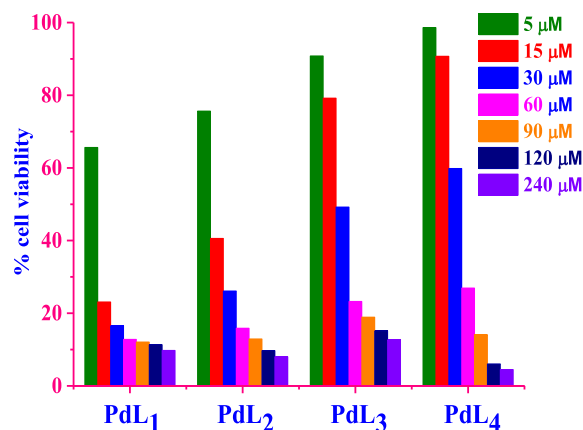

**Fig. 9.** Percentage of cell viability of MCF7 cells when treated for 24 h with different concentrations of **PdL1**–**4**.

Table 6
The IC$_{50}$ (μM) values of the complexes, **PdL1**–**4** towards the normal Vero and selected breast cancer MCF7 cell lines.

Complex	IC$_{50}$ (μM)	
	Normal Vero	Breast cancer MCF-7
PdL1	33 ± 3	4 ± 0.5
PdL2	48 ± 2	13 ± 1
PdL3	46 ± 2	27 ± 2
PdL4	34 ± 2	22 ± 2
Cisplatin	20 ± 9 (positive control)	5 ± 1 (positive control)

Data are calculated by mean ± standard deviation (SD) of three independent experiments, *i.e.*, $n = 3$, for 24 h of incubation.

in Fig. 9 while IC$_{50}$ values are presented in Table 6. Cell viability depended on the dose of the complexes, **PdL1**–**4**. The complexes are quite cytotoxic (with IC$_{50}$ values < 30 μM for the least potent) against aggressive MCT-7 breast cell lines. However, they are also very toxic
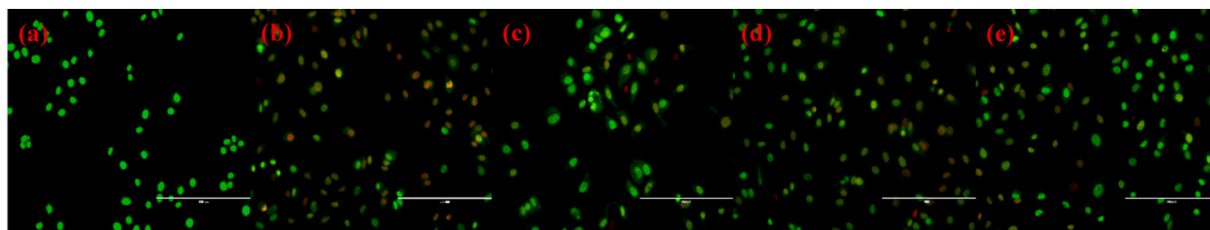
Fig. 10. AO/EB staining assay images of the MCF-7 cancer cell line after treatment with 10 μM of **PdL1**–**4** for 24 h, Images for **PdL1** (b); **PdL2** (c); **PdL3** (d) and **PdL4** (e). The images were visually compared with the negative control image (a).

against normal Vero, IC$_{50}$ < 50 μM for the least potent, see Table 6. Their indiscriminately cytotoxic to both cell types, including the normal healthy Vero cells precludes them for further *in vivo* tests. But note-worthy is that the terpyridyl complex, **PdL1** proved to be the most cytotoxic candidate against MCF7 cell lines. Its cytotoxicity was comparable but slightly lower than cisplatin's against this cancer cell line. The superior cytotoxicity of **PdL1** could be due to a combination of its more planar and unhindered geometry and stronger π-conjugation of its ligand framework; all of which cause favourable strong interactions with the DNA of the cancer cells. However, further testing on other breast cancer cell lines needs to be done to confirm its superior cytotoxicity in related cancer cell lines.

3.5.2. Cell morphology of MCF7 cells treated with complexes by the AO/EtBr staining assay

Morphological changes due to MCF7 cancer cells after a 24 h treatment of the cells with **PdL1**–**4** complexes at 10 μM were visualised by fluorescence microscopy, following staining with a solution of the AO/EtBr fluorescence marker. Images are depicted in Fig. 10b-e. Untreated MCF7 cancer cells (negative control, see Fig. 10a) showed characteristic green fluorescence which is associated with stained viability cells. Thus, no morphological changes were induced by components of the growth media. However, after a 24 h incubation of MCF7 cells treated with 10 μM of **PdL1**–**4**, cell stains had a significant orange-yellow hue, see Fig. 10b-e. Micrographic image of **PdL1** had the highest density of the non-green stains. This is a reflection of cell morphological changes synonymous with membrane blebbing and associated changes to the structure of normal nuclear DNA. These changes modulate the extent of intercalation of EtBr on the DNA and hence the hue of the fluorescence which is visualised on the microscope. Such changes are associated with the onset of early apoptotic cell damage. The orange hue is due to cells in their late apoptotic cell cycle stages. At these apoptotic stages, the chromatins of the cells are condensed and aggregated and thus stains appear as dense spots. The red colour fluorescence hue is due to dead cells, whose DNA had been necrosed. Overall, the results indicate that morphological changes associated with apoptotic cell cycles as well as necrosis [83] of the MCF7 cells had occurred at a significantly lower dose (10 μM) of the **PdL1**–**4**. This is in good agreement with very low (< 30 μM for the least active) IC$_{50}$ values measured *in vitro* by the MTT assay.

4. Conclusions

The rate of chloride substitution from complexes **PdL1**–**4** decreases in the order: **PdL1** > **PdL2** > **PdL3** ≫ **PdL4**. It can be explained mainly by electronic effects of the spectator ligands for complexes **PdL1**–**3**. The pyrazollic-N-π-donor effect of *cis*-coordinated pyrazoles in **PdL2**, decreases the ability of π-back bonding relative to that of **PdL1**, resulting in accumulation of electrons around the Pd-N$_{cis}$ bonds in **PdL2** and this lowers the electrophilicity of Pd, leading to reduced nucleophilic attack of the complex. A comparison of the structural differences between **PdL3** and **PdL4** points to the steric effects of the six-membered flexible chelates as well as to the steric hindrance by the methyl substituents on

the *cis*-coordinated pyrazoles of **PdL4** as plausible structural factors reducing the reactivity of the latter complex. The six-membered chelate rings incorporating the bridging sp^3 methylene carbons introduces steric hindrance and curtails π-back bonding of electron density into the ligand, resulting in lower rates of substitution. This significantly reduces the rate of substitution from **PdL4** by 4–6 orders of magnitude compared to the rate constants of **PdL1**. Reducing reactivity of Pd(II) metal complexes to a rate similar to those of Pt(II) through coordination of a suitable spectator ligands has been demonstrated. This is important in controlling indiscriminate deactivation reactions that are unwanted in antitumour and other biological application. The negative entropy of activation values show that the rate determining step in bimolecular and hence associative in nature.

UV–visible absorption, EtBr/CT-DNA competitive fluorescence titrations and viscosity measurements of the **PdL1**–**4** complexes collectively showed an associative binding of **PdL1**–**4** to DNA occurs with high binding constants ($K_b = 10^4$ M^{-1}). The increasing order of binding abilities of the complexes is **PdL4** < **PdL3** < **PdL2** < **PdL1**. Data obtained from *In vitro* cytotoxicity by the MTT assay pointed out **PdL1** to be the most cytotoxic complex (IC$_{50}$ = 4.0 ± 0.5 μM) against MCF7 cell lines. Its cytotoxicity against MCF7 was comparable but slightly lower than cisplatin's. AO/EB staining microscopy images of MCF7 cancer cells after a 24 h treatment with **PdL1**–**4** (*ca.* 10 μM) showed evidence of cell blebbing, induction of apoptosis in its early stages and cell death by necrosis.

Declaration of competing interest

There are no conflicts of interests to declare.

Appendix A. Supplementary data

Electronic Supplementary Information (ESI) available: Single X-ray crystallographic analysis were deposited with Cambridge Crystallographic Data Center, with reference numbers CCDC 1587601, 1587602 and 1829126 for the complexes; **PdL2**, **PdL3** and **PdL4**, respectively. Also, spectral (NMR and MS) characterization data for ligands and complexes and additional kinetic plots and data tables of the same are presented. In addition, notes of some procedures, DNA binding UV–visible and fluorescence spectra as well as crystallographic data in CIF are annexed. Supplementary data to this article can be found online at https://doi.org/10.1016/j.jinorgbio.2020.111261.

References

[1] Ž.D. Bugarčić, J. Bogojeski, R. van Eldik, Coord. Chem. Rev. 292 (2015) 91–106.
[2] D. Wang, S.J. Lippard, Nat. Rev. Drug Discov. 4 (2005) 307–320.
[3] S. van Zutphen, J. Reedijk, Coord. Chem. Rev. 249 (2005) 2845–2853.
[4] H. Zorbas, B.K. Keppler, ChemBioChem 6 (2005) 1157–1166.

[5] Ž.D. Bugarčić, J. Bogojeski, B. Petrović, S. Hochreuther, R. van Eldik, Dalton Trans. 41 (2012) 12329–12345.
[6] E. Alessio, Bioinorganic Medicinal Chemistry, John Wiley & Sons, 2011.
[7] Ž.D. Bugarčič, G. Liehr, R. van Eldik, J. Chem. Soc. Dalton Trans. (2002) 2825–2830.
[8] J. Reedijk, Chem. Rev. 99 (1999) 2499–2510.
[9] E.R. Jamieson, S.J. Lippard, Chem. Rev. 99 (1999) 2467–2498.
[10] B. Petrović, Ž.D. Bugarčić, A. Dees, I. Ivanović-Burmazović, F.W. Heinemann, R. Puchta, S.N. Steinmann, C. Corminboeuf, R. Van Eldik, Inorg. Chem. 51 (2012) 1516–1529.
[11] E. Wong, C.M. Giandomenico, Chem. Rev. 99 (1999) 2451–2466.
[12] M.E. Alberto, C. Cosentino, N. Russo, Struct. Chem. 23 (2012) 831–839.
[13] N.J. Farrer, L. Salassa, P.J. Sadler, Dalton Trans. (2009) 10690–10701.
[14] P. Blower, Dalton Trans. (2006) 1705–1711.
[15] X. Wang, Z. Guo, Dalton Trans. (2008) 1521–1532.
[16] S.P. Fricker, Dalton Trans. (2007) 4903–4917.
[17] S.P. Fricker, Metallomics 2 (2010) 366–377.
[18] M. Tanaka, H. Kataoka, S. Yano, H. Ohi, K. Kawamoto, T. Shibahara, T. Mizoshita, Y. Mori, S. Tanida, T. Kamiya, BMC Cancer 13 (2013) 237.
[19] M. Al-Noaimi, A.S. Abu-Surrah, L. Tahtamouni, Arab. J. Chem. 9 (2016) S1503–S1509.
[20] A.R. Kapdi, I.J. Fairlamb, Chem. Soc. Rev. 43 (2014) 4751–4777.
[21] M. Galanski, V. Arion, M. Jakupec, B. Keppler, Curr. Pharm. Des. 9 (2003) 2078–2089.
[22] A.S. Abu-Surrah, H.H. Al-Sa`doni, M.Y. Abdalla, Cancer Therapy 6 (2008) 1–10.
[23] T. Rau, R. van Eldik, Met. Ions Biol. Syst. 32 (1996) 339–378.
[24] Ž.D. Bugarčić, G. Liehr, R. van Eldik, J. Chem. Soc. Dalton Trans. (2002) 951–956.
[25] Z.D. Bugarcic, B. Petrovic, E. Zangrando, Inorg. Chim. Acta 357 (2004) 2650–2656.
[26] M. Marques, ISRN Spectroscopy 2013 (2013) 1–29.
[27] M. González, J. Tercero, A. Matilla, J. Niclós-Gutiérrez, M. Fernández, M. López, C. Alonso, S. González, Inorg. Chem. 36 (1997) 1806–1812.
[28] H. Mansuri-Torshizi, T. Srivastava, H. Parekh, M. Chitnis, J. Inorg. Biochem. 45 (1992) 135–148.
[29] J. Butoura, S. Wimmerb, F. Wimmerb, P. Castanc, Chem. Biol. Interact. 104 (1997) 165–178.
[30] A.S. Abu-Surrah, M. Kettunen, Curr. Med. Chem. 13 (2006) 1337–1357.
[31] J. Bogojeski, J. Volbeda, M. Freytag, M. Tamm, Ž.D. Bugarčić, Dalton Trans. 44 (2015) 17346–17359.
[32] N.P. Barry, P.J. Sadler, Chem. Commun. 49 (2013) 5106–5131.
[33] T. Al-Allaf, L. Rashan, Boll. Chim. Farm. 140 (2000) 205–210.
[34] S. Kern, P. Illner, S. Begel, R. van Eldik, Eur. J. Inorg. Chem. 2010 (2010) 4658–4666.
[35] P. Illner, S. Kern, S. Begel, R. van Eldik, Chem. Commun. 0 (2007) 4803–4805.
[36] D. Jaganyi, D. Reddy, J. Gertenbach, A. Hofmann, R. van Eldik, Dalton Trans. (2004) 299–304.
[37] A. Hofmann, L. Dahlenburg, R. van Eldik, Inorg. Chem. 42 (2003) 6528–6538.
[38] D. Jaganyi, K.L.D. Boer, J. Gertenbach, J. Perils, Int. J. Chem. Kinet. 40 (2008) 808–818.
[39] B. Pitteri, G. Marangoni, L. Cattalini, F. Visentin, V. Bertolasi, P. Gilli, Polyhedron 20 (2001) 869–880.
[40] P. Ongoma, D. Jaganyi, Dalton Trans. 41 (2012) 10724–10730.
[41] A. Shaira, D. Reddy, D. Jaganyi, Dalton Trans. 42 (2013) 8426–8436.
[42] D. Reddy, D. Jaganyi, Dalton Trans. (2008) 6724–6731.
[43] D. Reddy, K.J. Akerman, M.P. Akerman, D. Jaganyi, Transit. Met. Chem. 36 (2011) 593–602.
[44] I.M. Wekesa, D. Jaganyi, J. Coord. Chem. 69 (2016) 389–403.
[45] I.M. Wekesa, The Influence of Ligand Moiety on the Substitution Behaviour of Mononuclear Platinum (II) Complexes. A Detailed Kinetic and Mechanistic Study, School of Chemistry and Physics, University of KwaZulu-Natal, South Africa, 2014.
[46] D.L. Jameson, K.A. Goldsby, The Journal of Organic Chemistry 55 (1990) 4992–4994.
[47] G.S. Nyamato, M.G. Alam, S.O. Ojwach, M.P. Akerman, Appl. Organomet. Chem. 30 (2016) 89–94.
[48] A.A. Watson, D.A. House, P.J. Steel, Inorg. Chim. Acta 130 (1987) 167–176.
[49] T.V. Dalrymple, T.U.o.T.a.S.A. Chemistry, Synthesis and Characterization of Palladium(II) Complexes as Potential Antitumor Agents, University of Texas at San Antonio, 2007.
[50] S.A. Willison, H. Jude, R.M. Antonelli, J.M. Rennekamp, N.A. Eckert, J.A. Krause Bauer, W.B. Connick, Inorg. Chem. 43 (2004) 2548–2555.
[51] S.O. Ojwach, I.A. Guzei, J. Darkwa, S.F. Mapolie, Polyhedron 26 (2007) 851–861.
[52] G. Sheldrick, University of Göttingen, Göttingen, (2014).
[53] L.J. Farrugia, J. Appl. Crystallogr. 45 (2012) 849–854.
[54] M. Frisch, G. Trucks, H. Schlegel, G. Scuseria, M. Robb, J. Cheeseman, G. Scalmani, V. Barone, B. Mennucci, G. Petersson, Gaussian 09, Revision D. 01, Gaussian, Inc, Wallingford CT, 2009.
[55] P.J. Hay, W.R. Wadt, J. Chem. Phys. 82 (1985) 299–310.
[56] V. Barone, M. Cossi, J. Phys. Chem. A 102 (1998) 1995–2001.
[57] M. Cossi, N. Rega, G. Scalmani, V. Barone, J. Comput. Chem. 24 (2003) 669–681.
[58] C.-Y. Gao, X. Qiao, Z.-Y. Ma, Z.-G. Wang, J. Lu, J.-L. Tian, J.-Y. Xu, S.-P. Yan, Dalton Trans. 41 (2012) 12220–12232.
[59] R. Bellam, D. Jaganyi, A. Mambanda, R. Robinson, M.D. BalaKumaran, RSC Adv. 9 (2019) 31877–31894.
[60] G.K. Mutua, R. Bellam, D. Jaganyi, A. Mambanda, J. Coord. Chem. 72 (2019) 2931–2956.
[61] A. Wolfe, G.H. Shimer Jr., T. Meehan, Biochemistry 26 (1987) 6392–6396.
[62] O. Stern, M. Volmer, Z 20 (1919) 183–188.
[63] J.R. Lakowicz, Principles of fluorescence spectroscopy, in: Fluorescence Quenching: Theory and Applications, Springer Science & Business Media, 2013, pp. 53–126.
[64] C. Parker, W. Rees, Analyst 87 (1962) 83–111.
[65] T. Mosmann, J. Immunol. Methods 65 (1983) 55–63.
[66] U.V. Mallavadhani, N.R. Vanga, M.K. Jeengar, V. Naidu, Eur. J. Med. Chem. 74 (2014) 398–404.
[67] G.L. Eakins, J.S. Alford, B.J. Tiegs, B.E. Breyfogle, C.J. Stearman, J. Phys. Org. Chem. 24 (2011) 1119–1128.
[68] G. Intille, C. Pfluger, W. Baker, Journal of Crystal and Molecular Structure 3 (1973) 47–54.
[69] D. Jaganyi, A. Hofmann, R. van Eldik, Angew. Chem. Int. Ed. 40 (2001) 1680–1683.
[70] J.K. Burdett, Inorg. Chem. 14 (1975) 931–934.
[71] J.K. Burdett, Inorg. Chem. 16 (1977) 3013–3025.
[72] F. Schramm, R. Chandrasekar, Thomas A. Zevaco, Manfred Rudolph, Helmar Görls, Wolfgang Poppitz, M. Rube, Eur. J. Inorg. Chem. (2009) 53–61.
[73] D.L. Jameson, J.K. Blaho, K.T. Kruger, K.A. Goldsby, Inorg. Chem. 28 (1989) 4312–4314.
[74] J.M. Holland, J.A. McAllister, C.A. Kilner, M. Thornton-Pett, A.J. Bridgeman, M.A. Halcrow, J. Chem. Soc. Dalton Trans. (2002) 548–554.
[75] T. Astley, A.J. Canty, M.A. Hitchman, G.L. Rowbottom, B.W. Skelton, A.H. White, J. Chem. Soc. Dalton Trans. (1991) 1981–1990.
[76] K.L. Garner, L.F. Parkes, J.D. Piper, J.G. Williams, Inorg. Chem. 49 (2009) 476–487.
[77] A. Mijatović, J. Bogojeski, B. Petrović, Ž.D. Bugarčić, Inorg. Chim. Acta 383 (2012) 300–304.
[78] A. Hofmann, D. Jaganyi, O.Q. Munro, G. Liehr, R. van Eldik, Inorg. Chem. 42 (2003) 1688–1700.
[79] D. Jaganyi, F. Tiba, O.Q. Munro, B. Petrović, Ž.D. Bugarčić, Dalton Trans. (2006) 2943–2949.
[80] E. Largy, F. Hamon, F. Rosu, V. Gabelica, E. De Pauw, A. Guédin, J.L. Mergny, M.P. Teulade-Fichou, Chem Eur J 17 (2011) 13274–13283.
[81] M. Cory, D.D. McKee, J. Kagan, D. Henry, J.A. Miller, J. Am. Chem. Soc. 107 (1985) 2528–2536.
[82] M.P. Barrett, C.G. Gemmell, C.J. Suckling, Pharmacol. Ther. 139 (2013) 12–23.
[83] A.S. Tkachenko, A.I. Onishchenko, V.G. Gopkalov, T.V. Gorbach, E.A. Kharchenko, D.O. Sklyaruk, Medicine. Reviews 4 (2019) 32–37.